

Energy transfer driven brightening of MoS₂ by ultrafast polariton relaxation in microcavity MoS₂/hBN/WS₂ heterostructures

Received: 9 January 2024

Accepted: 29 January 2024

Published online: 26 February 2024

Check for updates

Zehua Hu ^{1,13}✉, Tanjung Krisnanda^{2,13}, Antonio Fieramosca^{3,13}, Jiaxin Zhao⁴, Qianlu Sun¹, Yuzhong Chen⁵, Haiyun Liu ⁵, Yuan Luo⁶, Rui Su ⁴, Junyong Wang ⁷, Kenji Watanabe ⁸, Takashi Taniguchi ⁹, Goki Eda ⁷, Xiao Renshaw Wang ^{4,10}, Sanjib Ghosh⁵, Kevin Dini⁴✉, Daniele Sanvitto³, Timothy C. H. Liew ⁴ & Qihua Xiong ^{5,6,11,12}✉

Energy transfer is a ubiquitous phenomenon that delivers energy from a blue-shifted emitter to a red-shifted absorber, facilitating wide photonic applications. Two-dimensional (2D) semiconductors provide unique opportunities for exploring novel energy transfer mechanisms in the atomic-scale limit. Herein, we have designed a planar optical microcavity-confined MoS₂/hBN/WS₂ heterojunction, which realizes the strong coupling among donor exciton, acceptor exciton, and cavity photon mode. This configuration demonstrates an unconventional energy transfer via polariton relaxation, brightening MoS₂ with a record-high enhancement factor of ~440, i.e., two-order-of-magnitude higher than the data reported to date. The polariton relaxation features a short characteristic time of ~1.3 ps, resulting from the significantly enhanced intra- and inter-branch exciton-exciton scattering. The polariton relaxation dynamics is associated with Rabi energies in a phase diagram by combining experimental and theoretical results. This study opens a new direction of microcavity 2D semiconductor heterojunctions for high-brightness polaritonic light sources and ultrafast polariton carrier dynamics.

Monolayer semiconducting transition metal dichalcogenides (TMDs) have recently emerged as a promising system in fundamental physics and technology-related studies of electronics, optoelectronics, valleytronics, and twistrionics. Their prominent properties are enabled by the weak dielectric screening, breaking of the inversion symmetry, and strong spin-orbit coupling^{1–4}. Despite being direct bandgap semiconductors, most monolayer TMDs exhibit poor photoluminescence (PL) yield due to the low absolute optical absorption of <10% as well as the low external quantum yield of <1%, which limits the development of nanophotonic devices such as light-emitting diodes (LEDs), lasers, display devices, and optical on-chip networks^{5–7}.

One prospective way to achieve a homogeneous enhancement of emission intensity is to deliver the excitation energy from the donor to the acceptor by nonradiative energy transfer. Conventional energy transfer comprises Förster resonance energy transfer (FRET) and Dexter-type energy transfer (DET); the former is based on dipole-dipole coupling (where the dipoles in the semiconductors are excitons), while the latter is based on charge transfer and spin conservation^{8–11}. To evaluate the effect of energy transfer, an enhancement factor (η) is usually defined as $\eta = I_{DA}/I_A$, where I_{DA} and I_A are the PL intensities of the acceptor in the heterojunction and on the bare substrate, respectively. For both FRET and DET in 2D

A full list of affiliations appears at the end of the paper. ✉ e-mail: zehuahu@nju.edu.cn; kdini@ntu.edu.sg; qihua_xiong@tsinghua.edu.cn

semiconductors, η is limited to ~ 2 to date^{8,10,12–14}. High-performance nanophotonic devices call for a new structure or mechanism for energy transfer with a colossal η to brighten 2D semiconductors.

Alternatively, for organic-semiconductor heterojunctions with Frenkel excitons, exciton-photon polaritons due to the strong coupling of excitons with microcavity provide a powerful platform to achieve unconventional energy transfer by polariton relaxation^{15–20}. In contrast, TMDs feature a more delocalized Wannier-Mott exciton nature^{21,22}. Their polaritons inherit the perfect in-plane dipole orientation, strong quantum confinement, and valley polarization, which provides more degree of freedoms to engineer new functionalities in the polariton field. Thus, TMDs polaritons have attracted great attention for the study of Bose-Einstein condensates^{23–25}, nonlinear optical processes^{26,27}, valley properties^{28–30}, LEDs³¹ as well as Moiré heterojunctions³². However, it remains elusive to realize the strong coupling of TMDs heterojunctions with microcavity for unconventional energy transfer due to the considerable challenge to avoid the PL quenching by ultrafast charge transfer and meanwhile to achieve the mode match among donor exciton, acceptor exciton, and cavity photon.

Here, by embedding the hBN/MoS₂/hBN/WS₂ heterojunction into a Fabry-Pérot (FP) microcavity, we have realized the strong coupling among the donor exciton, acceptor exciton, and cavity photon mode, which leads to the brightening of MoS₂ with a two-order-of-magnitude enhancement of PL yield ($\eta \approx 440$) based on the

exciton-photon polariton relaxation. The custom-designed k -space transient-reflectivity spectroscopy, which features a better spectral resolution than the real-space measurement for microcavity samples, was applied to evaluate the polariton relaxation dynamics, and a characteristic time as short as ~ 1.3 ps was extracted. The efficient and ultrafast polariton relaxation is associated with the significantly enhanced intra- and inter-branch exciton-exciton scattering, which overcomes the hot phonon bottleneck effect. Moreover, the phase diagram has been established to correlate the polariton relaxation efficiency with the Rabi energies. This study demonstrates a new branch of microcavity-confined 2D semiconductor heterojunctions with a great potential for ultrafast highly-bright polaritonic light sources.

Results

Sample fabrication and optical characterization

For the optical microcavity-confined heterojunction, the strong coupling among the acceptor's (E_{ex1}) and donor's (E_{ex2}) excitons as well as the cavity photon mode (E_c) will form the exciton-photon polariton with three anti-crossing eigenstates denoted by the upper (UPB), middle (MPB), and lower (LPB) polariton branches (Fig. 1a)^{15–19}. Under off-resonance optical excitation, the polariton tends to relax from the UPB to MPB and finally to LPB (i.e., from high energy and high in-plane momentum (k_{\parallel}) to low energy and low k_{\parallel}). The relaxation process is an unconventional energy transfer since the UPB and LPB are mostly E_{ex2} -

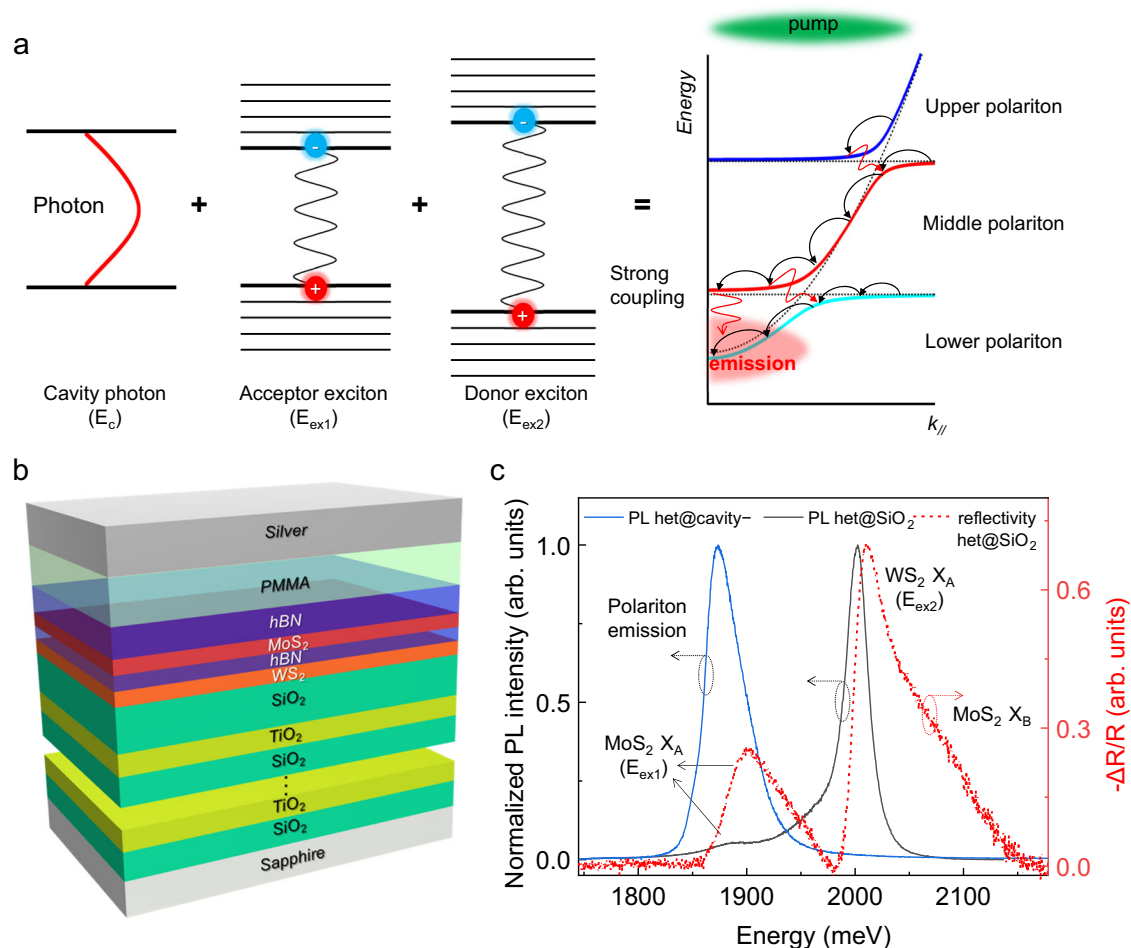


Fig. 1 | Design, construction, and properties of FP microcavity-confined hBN/MoS₂/hBN/WS₂ heterojunction. **a** Schematic formation and relaxation of exciton-photon polariton. The black and red arrows in the right panel represent intra- and inter-branch scattering, respectively. **b** Schematic illustration of microcavity-

confined hBN/MoS₂/hBN/WS₂ heterojunction. **c** Normalized real-space PL spectra of het@SiO₂ (black) and het@cavity- (blue). The differential reflection spectrum of het@SiO₂ (dashed red) is presented for reference. X_A and X_B are A and B exciton, respectively.

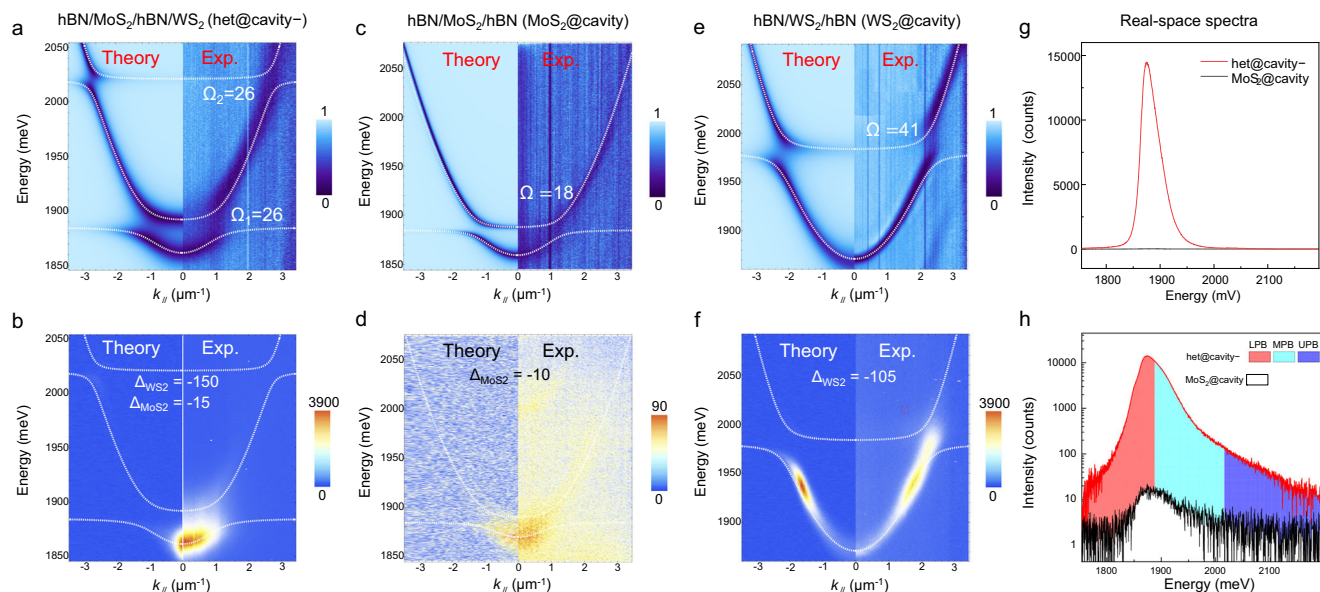


Fig. 2 | Comparison of polariton relaxations in **het@cavity-, **MoS₂@cavity** and **WS₂@cavity**.** **a, b** *k*-space energy-resolved reflectivity mapping (**a**), PL mapping (**b**) for **het@cavity-**. **c, d** The corresponding results for **MoS₂@cavity**. **e, f** The corresponding results for **WS₂@cavity**. The Rabi splitting (Ω) and exciton-photon

detuning (Δ) energies are labeled in the unit of meV. Note: data range of the color bar in (**d**) is much smaller than that in (**b**) and (**f**). **g, h** The real-space PL spectra of **het@cavity-** and **MoS₂@cavity** in linear (**g**), and log (**h**) scale under 10 μ W excitation.

like and E_{ex1} -like, respectively, as determined by the Hopfield coefficients^{15–19}.

The configuration of microcavity-confined heterojunction in this study is illustrated in Fig. 1b. The hBN/MoS₂/hBN/WS₂ heterojunction was fabricated by a pick-up method (Supplementary Fig. 1)³². WS₂ (donor) and MoS₂ (acceptor) are monolayers with a direct bandgap, while the top and middle hBN are 15 and 2 nm, respectively. The middle thin hBN layer prevents the ultrafast interlayer charge transfer from nonradiative recombination while keeping the FRET almost intact^{13,33,34}. Then, the heterojunction was transferred onto a bottom-distributed Bragg reflector (DBR) composed of 6.5 pairs of SiO₂ and TiO₂ dielectric layers, with its photonic stopband covering the heterojunction exciton energies (Supplementary Fig. 2). Subsequently, a poly(methyl methacrylate) (PMMA) spacer and a silver mirror were deposited to finalize the microcavity device. The thickness of PMMA spacer was adjusted to achieve the negative (positive) acceptor exciton-photon detuning, with the microcavity heterojunction labeled as **het@cavity-** (**het@cavity+**), respectively. Supplementary Table 1 summarizes the thickness information of **het@cavity-**, which ensures an energy match between the cavity mode and heterojunction excitons, i.e., the heterojunction placed in the maximum of the electromagnetic field. For quantitative comparison, an identical heterojunction was fabricated on a SiO₂(90 nm)-coated Si substrate to avoid the cavity effect, defined as **het@SiO₂** (Supplementary Fig. 3a).

Figure 1c compares the normalized real-space PL spectra of **het@cavity-** and **het@SiO₂**, with the differential reflection spectrum of **het@SiO₂** as a reference. The real-space PL spectrum of **het@SiO₂** features two emission peaks, i.e., A exciton (X_A) emission from WS₂ at 2002 meV and MoS₂ at 1890 meV, with a Stokes shift of -10 meV relative to the corresponding reflectivity spectrum. The PL intensity of WS₂ X_A is much stronger than that of MoS₂ X_A , which results from the higher intrinsic exciton dipole oscillator strength (f) and quantum yield of the former, and the interlayer FRET ($\eta \approx 3$), as detailed in Supplementary Fig. 3. On the contrary, the PL spectrum of **het@cavity-** is only composed of a single peak at 1873 meV, with the even smaller energy than the PL of MoS₂ X_A . The significant change

of PL spectra, in both shape and energy, points out the crucial effect of the optical microcavity confinement on energy transfer.

The energy transfer in **het@cavity-** is further understood by means of the *k*-space energy-resolved reflectivity and PL mappings, in comparison with the cases of microcavity-confined hBN/MoS₂/hBN (**MoS₂@cavity**) and hBN/WS₂/hBN (**WS₂@cavity**), as summarized in Fig. 2a–f. The polariton dispersions for **het@cavity-** are fitted with a three coupled oscillator model^{15–17}, i.e.,

$$\begin{pmatrix} E_c(\theta) & \Omega_2/2 & \Omega_1/2 \\ \Omega_2/2 & E_{\text{ex2}} & 0 \\ \Omega_1/2 & 0 & E_{\text{ex1}} \end{pmatrix} \begin{pmatrix} \alpha_c \\ \alpha_{\text{ex2}} \\ \alpha_{\text{ex1}} \end{pmatrix} = E_{\text{pol}}(\theta) \begin{pmatrix} \alpha_c \\ \alpha_{\text{ex2}} \\ \alpha_{\text{ex1}} \end{pmatrix} \quad (1)$$

where $E_c(k) = E_0(1 - \sin^2(\theta)/n^2)^{-1/2}$ is the cavity photon mode energy, θ is the angle of incidence, E_0 is the cavity cut off energy, and n is the cavity effective refractive index. E_{ex1} , E_{ex2} and $E_{\text{pol}}(\theta)$ are the energies of acceptor exciton, donor exciton, and polariton, respectively. Ω_1 and Ω_2 are the corresponding Rabi splitting energies. α_{ex1} , α_{ex2} and α_c are the corresponding Hopfield coefficients (Supplementary Fig. 4). The angle dependence of the three eigenvalues corresponds to three dispersion branches termed UPB, MPB, and LPB, respectively (the white dotted lines in Fig. 2a, b). Similarly, the polariton dispersions for **MoS₂@cavity** and **WS₂@cavity** are fitted with a two-coupled oscillator model, which gives two branches, termed UPB and LPB (see Method).

The reflectivity mappings of **MoS₂@cavity** and **WS₂@cavity** show two anti-crossing branches with Rabi splitting energy (Ω) of 18 and 41 meV, respectively (Fig. 2c, e), consistent with the smaller exciton dipole oscillator strength of MoS₂ than WS₂ ($\Omega \propto \sqrt{f}$, Supplementary Fig. 3b)^{35,36}. In contrast, **het@cavity-** features three branches with two anti-crossing points, demonstrating the strong coupling among MoS₂ exciton, WS₂ exciton, and cavity photon mode, with Ω_1 (Ω_2) \approx 26 (26) meV and a negative (negative) exciton-photon detuning (Δ) of -15 (-150) meV for MoS₂ (WS₂) (Fig. 2a). Ω_1 of **het@cavity-** is larger than Ω of **MoS₂@cavity** and Ω_2 of **het@cavity-** is smaller than Ω of **WS₂@cavity**, which straightforwardly indicates the transfer of dipole oscillator strength from E_{ex2} to E_{ex1} ³⁷. A similar transfer is also reflected in **het@cavity+** with a Ω_1 (Ω_2) \approx 42 (24) meV and a positive (negative) Δ of +13 (-132) meV for MoS₂ (WS₂) (Supplementary Fig. 5a). These

results suggest a general feature of the transfer of dipole oscillator strength in the strongly coupled microcavity-confined heterojunctions, in sharp contrast to the negligible transfer in the cavity-free het@SiO₂ counterpart (Supplementary Fig. 3b). The experimental reflectivity mappings are well-reproduced by theoretical calculation with the transfer matrix method (Fig. 2a, c, e, detailed in Supplementary part III)^{38–40}.

The PL mapping of MoS₂@cavity suffers from a weak polariton emission due to the weak dipole oscillator strength and low quantum yield of MoS₂ (Fig. 2d)⁵, while that of WS₂@cavity suffers from a hot phonon bottleneck effect (the broad emission centred at -1.7 μm⁻¹) due to the large negative Δ (-105 meV, Fig. 2f)^{29,41,42}. On the contrary, the PL mapping of het@cavity- integrates the advantages of MoS₂@cavity and WS₂@cavity, i.e., inherits the narrow linewidth from MoS₂@cavity and high intensity from WS₂@cavity (Fig. 2b); so does the PL mapping of het@cavity+ (Supplementary Fig. 5b). The PL intensity of het@cavity- in real-space photoluminescence excitation spectrum increases monotonously without resonance peak when decreasing the excitation energy towards LPB (Supplementary Fig. 6). The preceding results confirm the energy transfer mechanism of polariton relaxation, rather than FRET or DET, in the strongly coupled microcavity-confined heterojunctions. In the linear-scale real-space PL spectrum, het@cavity- and MoS₂@cavity show bright and negligible emission under 10 μW excitation, respectively (Fig. 2g). From Fig. 2b, it is learned that the polariton emission of het@cavity- comes from the LPB and MPB with |k_∥| < 1.6 μm⁻¹, which is composed of MoS₂ exciton and cavity photon but negligible WS₂ exciton (Supplementary Fig. 4a). Hence, η is obtained to be ~440 from the ratio of $I_{\text{het@cavity-}}^{\text{LPB+MPB}} / I_{\text{MoS}_2\text{@cavity}}^{\text{LPB+UPB}}$. Here $I_{\text{het@cavity-}}^{\text{LPB+MPB}}$ and $I_{\text{MoS}_2\text{@cavity}}^{\text{LPB+UPB}}$ are the integrated polariton emission intensity from LPB+MPB (red+cyan region) of het@cavity- and LPB+UPB of MoS₂@cavity (black-outlined region) in real-space, respectively (Fig. 2h, detailed in Supplementary Note 1). As summarized in Supplementary Table 2, the giant η of 440 for het@cavity- is over 146 times larger than the η of 3 with FRET for het@SiO₂ counterpart, also two orders of magnitude higher than the typical η of FRET or DET processes in literature, demonstrating a powerful strategy to significantly increase the energy transfer efficiency by polariton relaxation.

Supplementary Figs. 7 and 8 show the optical characteristics of the additional microcavity-confined heterojunction samples, specifically identified as het8@cavity (8 nm hBN), het2@node@cavity (heterojunction with 2 nm hBN at the node), and het60@cavity (60 nm hBN). These diverse configurations, characterized by different heterojunction's positions within the cavity and/or different thicknesses of hBN, give rise to distinct Rabi energies Ω₁ and Ω₂. Consequently, the distinct Rabi energies lead to a substantial difference in polariton relaxation efficiency. This result demonstrates the crucial role of Rabi energies in polariton-mediated energy transfer, which has not been recognized to date and will be further theoretically clarified later.

Theoretical simulation

We simulated the *k*-space PL mappings with the coupled rate equations^{43–46}, which describe the dynamics of polariton populations in different branches. The different points with the different relative excitonic and photonic fractions in *k*-space for each branch are identified by the coupled oscillator model and the Hopfield coefficients (Supplementary Fig. 4). The coupled rate equations for het@cavity- with three polariton branches read

$$\frac{dN_j^\Xi}{dt} = (P_1 X_{1j}^\Xi + P_2 X_{2j}^\Xi - \gamma C_j^\Xi) N_j^\Xi + \sum_{\Xi'} S^{\Xi\Xi'} \quad (2)$$

where N_j^Ξ is the polariton population, $\Xi = \{U, M, L\}$ corresponds to the UPB, MPB, and LPB, 1 (2) indicates MoS₂ (WS₂), and index *j* denotes the

respective point in *k*-space. $P_{1(2)}$ stands for an effective pumping for the exciton, and γ for the decay rate of the photon mode. Here, $P_2 > P_1$ due to the much brighter polariton emission of WS₂@cavity than MoS₂@cavity (Fig. 2d, f). The $X_{1(2)}^\Xi$ and C^Ξ denote $|\alpha_{1(2)}^\Xi|^2$ and $|\alpha_c^\Xi|^2$ (Supplementary Fig. 4). The relaxation processes, described by the last term in (2), consist of the intra- and inter-branch transitions originating from the phonon-mediated exciton scattering^{47,48}. In this formalism, the preferred transition with a high rate happens between initial and final destinations with high $X_1^\Xi X_1^{\Xi'}$, $X_2^\Xi X_2^{\Xi'}$ and phonon population $n_{ph}(E_{ph})$. According to Bose distribution function, i.e., $n_{ph} = \frac{1}{\exp(\frac{E_{ph}}{k_B T}) - 1}$ (here $E_{ph} = |E^\Xi - E^{\Xi'}|$), n_{ph} is large for transitions with close energies. The photonic part of the numerical steady-state solution for N_j^Ξ , together with an added Gaussian broadening, agrees with our experimental result (Fig. 2b, d, f; Supplementary part III for details).

Specifically, for MoS₂@cavity, P_1 excites the population in the low- (high-) *k*_∥ region of UPB (LPB) with high exciton fractions $X_1^U (X_1^L)$ (Supplementary Fig. 4b). The population will relax by the inter-branch scattering (from UPB to LPB) due to the high $X_1^U X_1^L$ at the anti-crossing point and the high $n_{ph} (E_{ph} \approx \Omega \approx 18 \text{ meV})$, followed by the intra-branch scattering (within LPB) due to the non-negligible $X_1^L X_1^L$ and the high n_{ph} (flat dispersion)^{47,48}. However, the polariton emission is considerably weak due to the weak oscillator strength and low quantum yield of MoS₂ exciton (Supplementary Fig. 3). For WS₂@cavity, P_2 also excites the population in the low- (high-) *k*_∥ region of UPB (LPB) with high exciton fractions $X_2^U (X_2^L)$ (Supplementary Fig. 4c). However, only a tiny portion of the population will relax to the bottom of LPB due to the poor inter-branch scattering for the low $n_{ph} (E_{ph} \approx \Omega \approx 41 \text{ meV})$ and the poor intra-branch scattering for the negligible $X_2^L X_2^L$, presenting the troublesome hot phonon bottleneck (Fig. 2f)^{29,41}.

Based on the above experimental and theoretical results, the polariton relaxation in het@cavity- could be well elucidated (Fig. 2b). Due to $P_2 > P_1$, P_2 excites the most population in the *k*_∥ < 2.5 (>2.5) μm⁻¹ region of UPB (MPB) with high $X_2^U (X_2^M)$ (Supplementary Fig. 4a). The population will relax by the inter-branch scattering (from UPB to MPB) due to the high $X_2^U X_2^M$ at the top anti-crossing point and the high $n_{ph} (E_{ph} \approx \Omega_2 \approx 26 \text{ meV})$. The subsequent intra-branch scattering within MPB is faster than that within LPB for WS₂@cavity due to the non-negligible $X_2^M X_2^M$ and $X_1^M X_1^M$ for the former compared to the negligible $X_2^L X_2^L$ for the latter. The synergism of the two scatterings leads to a fast relaxation of almost all the population to the bottom anti-crossing point. The population will further relax towards the bottom of LPB in a way similar to that in MoS₂@cavity, as reflected in Fig. 1a. Such a fast polariton relaxation dynamics leads to the bright PL of het@cavity- at the bottom of LPB (Fig. 2b).

Dynamics and phase diagram

With a custom-designed microscopic *k*-space transient-reflectivity spectroscopy (see Methods), we have simultaneously unravelled the evolution of the polariton population in momentum, energy and time domains. After being pumped by a 200-fs laser pulse of -2 μW at 580 nm, the change of reflectivity ($\frac{\Delta R}{R} = \frac{R_{\text{pump on}} - R_{\text{pump off}}}{R_{\text{pump off}}}$) of the broadband white light is measured after a specific time delay, where $R_{\text{pump on}}$ and $R_{\text{pump off}}$ are the reflectivity mappings with or without optical pumping, respectively. Such an excitation fluence is low enough to avoid exciton-exciton annihilation^{49,50}. The *k*-space transient-reflectivity spectroscopy results of WS₂@cavity and het@cavity- are shown in Fig. 3, with the corresponding movies in Supplementary Material. For the WS₂@cavity, the laser pulse excites the exciton reservoir to quickly form polaritons, which induces a net photobleaching signal at 0 ps at *k*_∥ ≈ 2.3 μm⁻¹ (Fig. 3a), also demonstrated in the integrated Δ*R*/*R* at *k*_∥ from 2.1 to 2.7 μm⁻¹ (Supplementary Fig. 9). Then, a derivative signal emerges at *k*_∥ ≈ 0 μm⁻¹ region, as clarified by

the integrated $\Delta R/R$ at $k_{\parallel} = 0 - 0.33 \mu\text{m}^{-1}$ (Fig. 3a, b and the movie in Supplementary Material). Such a signal represents the blue-shift of LPB due to the polariton-polariton repulsive interaction or the phase-space-filling effect of exciton (Supplementary Figs. 10, 11)⁵¹. The signal intensity gradually increases, reaches the maximum at -6 ps, and slowly decays afterward (Fig. 3a). By fitting the evolution of the derivative signal with the rising function ($y = A + B \operatorname{erf}(t/\tau)$, where $\operatorname{erf}(z) = \frac{2}{\sqrt{\pi}} \int_0^z e^{-t^2} dt$), a characteristic rising time (τ) of -2.8 ± 0.4 ps is obtained (Fig. 3c)⁵². In contrast, for *het@cavity-*, the intensity of the derivative signal at $k_{\parallel} \approx 0 \mu\text{m}^{-1}$ region increases much faster and reaches the maximum at -2 ps (Fig. 3d, e). With the same fitting method, a much shorter τ of -1.3 ± 0.2 ps is obtained (Fig. 3f), which approximates to the τ of 1.2 ± 0.2 ps in *MoS₂@cavity* (Supplementary Fig. 12). Therefore, *het@cavity-* demonstrates the ultrafast energy

transfer processes accompanied by the highest enhancement factor (440) to date (Supplementary Table 2).

Based on the preceding qualitative and quantitative analysis, we have formulated the phase diagram that correlates the polariton relaxation efficiency and characteristic rising time with the Rabi energies Ω_1 and Ω_2 , as shown in Fig. 4 (see Supplementary part III for details). Here we define a measure of efficiency as the sum of the photonic part of LPB population in the steady-state, *i.e.*, $\mathcal{N}(\tau_s) \equiv \sum N_j^L(\tau_s) C_j^L$ only for low- k_{\parallel} points (τ_s denotes the time at steady state). In general, $\mathcal{N}(\tau_s)$ monotonously increases with decreasing Ω_2 (except for $\Omega_2 \rightarrow 0$) due to the enhanced interbranch scattering between UPB and MPB. For a specific Ω_2 , $\mathcal{N}(\tau_s)$ depends on the trade-off between the intra-branch scattering in MPB and the inter-branch scattering (MPB to LPB), hence a suitable Ω_1 is needed for the optimal $\mathcal{N}(\tau_s)$ as

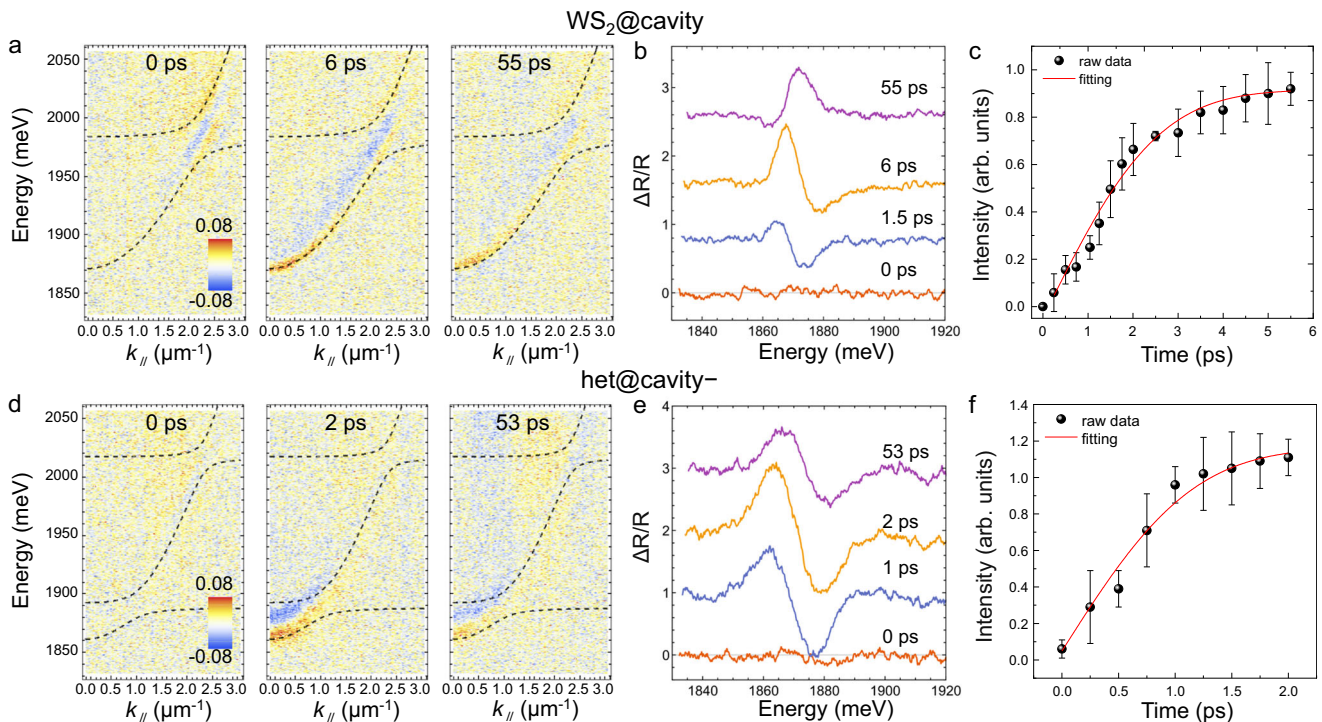


Fig. 3 | Time-resolved polariton relaxation dynamics. **a–c** *k*-space transient-reflectivity spectroscopy mapping (**a**), the integrated $\Delta R/R$ in $0 - 0.33 \mu\text{m}^{-1}$ at typical time delays (**b**), and the intensity evolution of the derivative signal (**c**) of

WS₂@cavity. **d–f** The corresponding data of *het@cavity-*. Note: The steady-state polariton branches are shown in dashed black to guide the reading. The error bars in (**c**) and (**f**) correspond to the standard error of the data points.

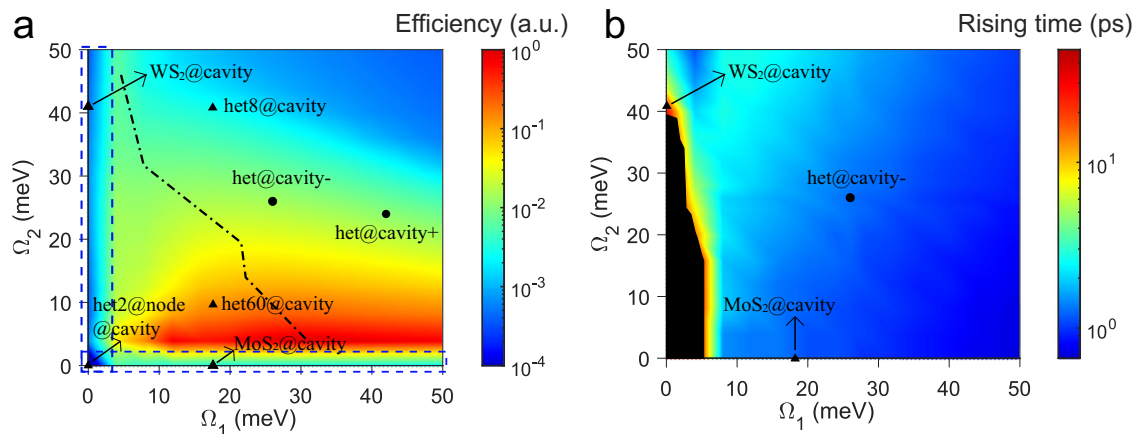


Fig. 4 | Phase diagram of the polariton relaxation dynamics versus Rabi energies. **a, b** Polariton relaxation efficiency (**a**) and characteristic rising time (**b**) with respect to Rabi energies Ω_1 and Ω_2 . The seven specific experimental cases are

marked. In **a**, the dashed-dotted curve indicates the optimal efficiency concerning Ω_1 and Ω_2 , and the dashed blue boxes show regions where $\Omega_1, \Omega_2 \rightarrow 0$. Note: In the dark area of **b**, the population in the low- k_{\parallel} region of LPB does not rise initially.

marked by the dashed-dotted curve (Fig. 4a). For the $\mathcal{N}(\tau_s)$ of specific cases, the het@cavity-, het@cavity+ and het60@cavity feature high efficiency. In contrast, $\mathcal{N}(\tau_s)$ is low for $\Omega_2 \rightarrow 0$ or $\Omega_1 \rightarrow 0$ (such as MoS₂@cavity, WS₂@cavity, and het2@node@cavity), or Ω_1 and Ω_2 are both large (such as het8@cavity), in agreement with the experimental results. Such an agreement offers a deep insight into the polariton-mediated energy transfer, which is inherently dominated by the Rabi energies.

Different from the $\mathcal{N}(\tau_s)$, the characteristic rising time is closely related to the scattering rate rather than the final polariton population in the low- k_{\parallel} region of LPB (Fig. 4b). After a Gaussian effective pump with amplitudes $\{P_1, P_2\}/50\gamma$, the evolution of the photonic part of the LPB population, i.e., $\mathcal{N}(t) \equiv \sum N_j^{\dagger}(t)C_j^{\dagger}$, is fitted by the rising function. For (Ω_1, Ω_2) located in the dark region, the negligible polariton fraction in the low- k_{\parallel} region of LPB prevents $\mathcal{N}(t)$ from growing. For $\Omega_1 \geq 8$ meV, the rising time monotonously decreases with increasing Ω_1 , which can be attributed to the dominant intra-branch scattering for the flatter LPB dispersion. Although the larger Ω_1 means the less transition from MPB to LPB, once the population relaxes to LPB, the strong intra-branch scattering leads to the faster relaxation to low- k points. It is worth noting that the faster rising time might not end up with a higher $\mathcal{N}(\tau_s)$, as evidenced by the comparison in Fig. 4a and Fig. 4b. The dependence of the rising time on Ω_2 is associated with the supply of population that will later end up in the low- k_{\parallel} region of LPB. Smaller Ω_2 results in more population relaxation from UPB to MPB, which allows faster growth of $\mathcal{N}(t)$, as supported by the longer rising time of WS₂@cavity than het@cavity- and MoS₂@cavity (Fig. 4b), in agreement with the experimental result (Fig. 3).

Discussion

In summary, we have successfully designed and constructed a planar optical microcavity-confined MoS₂/hBN/WS₂ heterojunction, in which the middle insulating hBN prevents the charge transfer-induced PL quenching. Such a configuration realizes the strong coupling among donor exciton, acceptor exciton and cavity photon mode, which results in the unconventional energy transfer mechanism of polariton relaxation in 2D material heterojunctions for the first time. Consequently, we have brightened the MoS₂ with the record-high energy transfer enhancement factor of ~440, which is two-order-of-magnitude higher than the data reported to date. A short characteristic time of ~1.3 ps is extracted for the ultrafast polariton relaxation dynamics, resulting from the significantly enhanced intra- and inter-branch exciton-exciton scattering to overcome the hot phonon bottleneck effect. The formulated phase diagram in this study establishes the correlation between the polariton relaxation dynamics and Rabi energies, which deepens the understanding on the underlying physics. This study drives the collaborative development of energy transfer and polariton fields toward the new topics of dark exciton energy transfer, valley-polarized energy transfer, and high-brightness ultrafast polaritonic light sources.

Methods

Sample fabrication

The bottom DBR was deposited on a sapphire substrate by using an e-beam evaporator (Cello, Ohmiker-50B), and was composed of 6.5 alternating pairs of titanium dioxide (TiO₂, $n=2.498$) and silicon dioxide (SiO₂, $n=1.478$). The hBN/MoS₂/hBN/WS₂ heterojunctions were fabricated using a dry-transfer method with a polypropylene carbonate (PPC) stamp. Monolayer WS₂, monolayer MoS₂, and thin hBN flakes were exfoliated onto silicon substrates with a 90-nm SiO₂ layer. A PPC stamp was used to pick up the flakes in sequence by a home-built micro-transfer stage (Supplementary Fig. 1). Then, the heterojunction was released to the DBR substrate, immersed in acetone overnight to remove the PPC, and annealed in a high vacuum ($<10^{-6}$ mbar) at 200 °C for 2 hours. The top PMMA layer was spin-

coated and the top silver mirror was deposited by a thermal evaporator.

Two coupled oscillator model

Similar to het@cavity-, the polariton dispersion in MoS₂@cavity and WS₂@cavity can be fitted with two coupled oscillator model,

$$\begin{pmatrix} E_c(\theta) & \Omega/2 \\ \Omega/2 & E_{ex} \end{pmatrix} \begin{pmatrix} \alpha_c \\ \alpha_{ex} \end{pmatrix} = E_{pol}(\theta) \begin{pmatrix} \alpha_c \\ \alpha_{ex} \end{pmatrix}$$

where E_{ex} is the energy of exciton, Ω the corresponding Rabi splitting energy. $|\alpha_c|^2$, $|\alpha_{ex}|^2$ are the Hopfield coefficients describing the photonic and excitonic weightings of the polaritons.

Optical characterization

The real-space steady-state PL and reflectivity spectra were conducted in a confocal spectrometer (Horiba Evolution 800) by using a CW laser (532 nm). K-space energy-resolved reflectivity and PL mapping were measured in a home-built setup with the Fourier imaging configuration with a high numerical aperture 100× microscope objective (NA = 0.9). The PL mappings are excited by a 532 nm continuous-wave (CW) laser of ~100 μW. The emission from the microcavity was collected through the narrow entrance slit of the spectrometer (Horiba iHR550) and finally onto the 2D charge-coupled device (CCD) array (Horiba, Symphony II). In the k-space transient-reflectivity spectroscopy measurement, the excitation pulsed laser was taken from a Ti:Sapphire laser equipped with an ultrafast amplifier (Spectra-Physics) and a computer-controlled Optical Parametric Amplifier (1 kHz repetition rate, with a roughly 200 fs pulse width). The output beam was split into two paths. One beam excited the sample almost at normal incidence to serve as the pump beam. The second beam went through a mechanical delay stage (Newport, M-ILS 150CC DC Servo Linear Stage) and a sapphire crystal to generate a delayed continuum light to serve as the probe pulse. The spot size of the pump and probe beams was around 2 μm and 3 μm, respectively. PLE spectra were obtained with a super-continuum light acting as the excitation source which is coupled to a monochromator. The excitation intensity was kept below 10 μW. A 655 nm long-pass filter was used to cut off the excitation photon that backscattered from the sample. All the measurements were carried out in a reflection configuration.

Data availability

All data needed to evaluate the conclusions in the paper are present in the paper and/or the Supplementary Materials. Additional data related to this paper may be requested from the authors.

References

1. Chhowalla, M., Jena, D. & Zhang, H. Two-dimensional semiconductors for transistors. *Nat. Rev. Mater.* **1**, 1–15 (2016).
2. Liu, Y., Huang, Y. & Duan, X. Van der Waals integration before and beyond two-dimensional materials. *Nature* **567**, 323–333 (2019).
3. Novoselov, K., Mishchenko, A., Carvalho, A. & Neto, A. C. 2D materials and van der Waals heterostructures. *Science* **353**, aac9439 (2016).
4. Seyler, K. L. et al. Signatures of moire-trapped valley excitons in MoSe₂/WSe₂ heterobilayers. *Nature* **567**, 66–70 (2019).
5. Amani, M. et al. Near-unity photoluminescence quantum yield in MoS₂. *Science* **350**, 1065–1068 (2015).
6. Wang, Z. et al. Giant photoluminescence enhancement in tungsten-diselenide-gold plasmonic hybrid structures. *Nat. Commun.* **7**, 1–8 (2016).
7. Mak, K. F., Lee, C., Hone, J., Shan, J. & Heinz, T. F. Atomically thin MoS₂: a new direct-gap semiconductor. *Phys. Rev. Lett.* **105**, 136805 (2010).

8. Kozawa, D. et al. Evidence for fast interlayer energy transfer in MoSe₂/WS₂ heterostructures. *Nano Lett.* **16**, 4087–4093 (2016).
9. Jin, C. et al. Ultrafast dynamics in van der Waals heterostructures. *Nat. Nanotechnol.* **13**, 994–1003 (2018).
10. Wu, L., Chen, Y., Zhou, H. & Zhu, H. Ultrafast energy transfer of both bright and dark excitons in 2D van der Waals heterostructures beyond dipolar coupling. *ACS Nano* **13**, 2341–2348 (2019).
11. Hu, Z. et al. Interfacial charge and energy transfer in van der Waals heterojunctions. *InfoMat* **4**, e12290 (2022).
12. Zhang, L. et al. Efficient and layer-dependent exciton pumping across atomically thin organic-inorganic type-I heterostructures. *Adv. Mater.* **30**, e1803986 (2018).
13. Hu, Z. et al. Trion-mediated Förster resonance energy transfer and optical gating effect in WS₂/hBN/MoSe₂ heterojunction. *ACS Nano* **14**, 13470–13477 (2020).
14. Meng, Y. et al. Electrical switching between exciton dissociation to exciton funneling in MoSe₂/WS₂ heterostructure. *Nat. Commun.* **11**, 2640 (2020).
15. Coles, D. M. et al. Polariton-mediated energy transfer between organic dyes in a strongly coupled optical microcavity. *Nat. Mater.* **13**, 712–719 (2014).
16. Zhong, X. et al. Non-radiative energy transfer mediated by hybrid light-matter states. *Angew. Chem. Int. Ed.* **55**, 6202–6206 (2016).
17. Zhong, X. et al. Energy transfer between spatially separated entangled molecules. *Angew. Chem. Int. Ed.* **56**, 9034–9038 (2017).
18. Lidzey, D. G., Bradley, D. D., Armitage, A., Walker, S. & Skolnick, M. Photon-mediated hybridization of Frenkel excitons in organic semiconductor microcavities. *Science* **288**, 1620–1623 (2000).
19. Georgiou, K., Jayaprakash, R., Othonos, A. & Lidzey, D. G. Ultralong-range polariton-assisted energy transfer in organic microcavities. *Angew. Chem. Int. Ed.* **60**, 16661–16667 (2021).
20. Garcia-Vidal, F. J. & Feist, J. Long-distance operator for energy transfer. *Science* **357**, 1357–1358 (2017).
21. Liu, X. et al. Control of coherently coupled exciton polaritons in monolayer tungsten disulphide. *Phys. Rev. Lett.* **119**, 027403 (2017).
22. Zhao, J., Zhao, W., Du, W., Su, R. & Xiong, Q. Dynamics of exciton energy renormalization in monolayer transition metal disulfides. *Nano Res* **13**, 1399–1405 (2020).
23. Anton-Solanas, C. et al. Bosonic condensation of exciton-polaritons in an atomically thin crystal. *Nat. Mater.* **20**, 1233 (2021).
24. Wurdack, M. et al. Motional narrowing, ballistic transport, and trapping of room-temperature exciton polaritons in an atomically thin semiconductor. *Nat. Commun.* **12**, 5366 (2021).
25. Zhao, J. et al. Ultralow threshold polariton condensate in a monolayer semiconductor microcavity at room temperature. *Nano Lett.* **21**, 3331–3339 (2021).
26. Zhao, J. et al. Nonlinear polariton parametric emission in an atomically thin semiconductor based microcavity. *Nat. Nanotechnol.* **17**, 1–7 (2022).
27. Zhao, J. et al. Exciton polariton interactions in Van der Waals superlattices at room temperature. *Nat. Commun.* **14**, 1512 (2023).
28. Chen, Y.-J., Cain, J. D., Stanev, T. K., Dravid, V. P. & Stern, N. P. Valley-polarized exciton-polaritons in a monolayer semiconductor. *Nat. Photon.* **11**, 431–435 (2017).
29. Sun, Z. et al. Optical control of room-temperature valley polaritons. *Nat. Photon.* **11**, 491–496 (2017).
30. Dufferwiel, S. et al. Valley-addressable polaritons in atomically thin semiconductors. *Nat. Photon.* **11**, 497–501 (2017).
31. Gu, J., Chakraborty, B., Khatoniar, M. & Menon, V. M. A room-temperature polariton light-emitting diode based on monolayer WS₂. *Nat. Nanotechnol.* **14**, 1024–1028 (2019).
32. Zhang, L. et al. Van der Waals heterostructure polaritons with moire-induced nonlinearity. *Nature* **591**, 61–65 (2021).
33. Liu, X. et al. Manipulating charge and energy transfer between 2D Atomic layers via heterostructure engineering. *Nano Lett.* **20**, 5359–5366 (2020).
34. Hong, X. et al. Ultrafast charge transfer in atomically thin MoS₂/WS₂ heterostructures. *Nat. Nanotechnol.* **9**, 682–686 (2014).
35. Skolnick, M., Fisher, T. & Whittaker, D. Strong coupling phenomena in quantum microcavity structures. *Semicond. Sci. Technol.* **13**, 645 (1998).
36. Agranovich, V. M., Litniskaia, M. & Lidzey, D. G. Cavity polaritons in microcavities containing disordered organic semiconductors. *Phys. Rev. B* **67**, 085311 (2003).
37. Sliotzky, M., Liu, X., Menon, V. M. & Forrest, S. R. Room temperature Frenkel-Wannier-Mott hybridization of degenerate excitons in a strongly coupled microcavity. *Phys. Rev. Lett.* **112**, 076401 (2014).
38. Vladimirova, M., Kavokin, A. & Kaliteevski, M. Dispersion of bulk exciton polaritons in a semiconductor microcavity. *Phys. Rev. B* **54**, 14566 (1996).
39. Kavokin, A. V., Baumberg, J. J., Malpuech, G. & Laussy, F. P. *Microcavities*. (Oxford University Press, 2017).
40. Krisnanda, T. et al. Room temperature light-mediated long-range coupling of excitons in perovskites. *Adv. Opt. Mater.* **9**, 2001835 (2021).
41. Coles, D. M., Grant, R. T., Lidzey, D. G., Clark, C. & Lagoudakis, P. G. Imaging the polariton relaxation bottleneck in strongly coupled organic semiconductor microcavities. *Phys. Rev. B* **88**, 121303 (2013).
42. Müller, M., Bleuse, J., Andre, R. & Ulmer-Tuffigo, H. Observation of bottleneck effects on the photoluminescence from polaritons in II–VI microcavities. *Phys. B: Condens.* **272**, 476–479 (1999).
43. Amthor, M. et al. Optical bistability in electrically driven polariton condensates. *Phys. Rev. B* **91**, 081404 (2015).
44. Solnyshkov, D., Terças, H., Dini, K. & Malpuech, G. Hybrid Boltzmann–Gross–Pitaevskii theory of Bose–Einstein condensation and superfluidity in open driven-dissipative systems. *Phys. Rev. A* **89**, 033626 (2014).
45. Zhang, Q. et al. Electric field modulation of 2D perovskite excitonics. *J. Phys. Chem. Lett.* **13**, 7161–7169 (2022).
46. Lyons, T. P. et al. Giant effective Zeeman splitting in a monolayer semiconductor realized by spin-selective strong light-matter coupling. *Nat. Photon.* **16**, 632–636 (2022).
47. Tassone, F., Piermarocchi, C., Savona, V., Quattropani, A. & Schwendimann, P. Bottleneck effects in the relaxation and photoluminescence of microcavity polaritons. *Phys. Rev. B* **56**, 7554 (1997).
48. Tassone, F. & Yamamoto, Y. Exciton-exciton scattering dynamics in a semiconductor microcavity and stimulated scattering into polaritons. *Phys. Rev. B* **59**, 10830 (1999).
49. Sun, D. et al. Observation of rapid exciton-exciton annihilation in monolayer molybdenum disulfide. *Nano Lett.* **14**, 5625–5629 (2014).
50. Yuan, L. & Huang, L. Exciton dynamics and annihilation in WS₂ 2D semiconductors. *Nanoscale* **7**, 7402–7408 (2015).
51. Gu, J. et al. Enhanced nonlinear interaction of polaritons via excitonic Rydberg states in monolayer WSe₂. *Nat. Commun.* **12**, 2269 (2021).
52. Giovanni, D. et al. Coherent spin and quasiparticle dynamics in solution-processed layered 2D lead halide perovskites. *Adv. Sci.* **5**, 1800664 (2018).

Acknowledgements

Z.H. gratefully acknowledges the National Key R&D Program of China (Grant No. 2022YFA1204301). Q.X. gratefully acknowledges funding support from the National Key Research and Development Program of China (Grant No. 2022YFA1204700), strong funding support from the

National Natural Science Foundation of China (Grant No. 12250710126), and strong support from the Tsinghua University Initiative Scientific Research Program. H.L. gratefully acknowledges funding support from the National Natural Science Foundation of China (Grant No. 92056204). S.G. acknowledges the funding support from the National Natural Science Foundation of China (Grant No. 12274034). D.S. and A.F. acknowledge the funding support from: “Quantum Optical Networks based on Exciton-polaritons”, (Q-ONE, N. 101115575, HORIZON-EIC-2022-PATHFINDER CHALLENGES EU project), “National Quantum Science and Technology Institute” (NQSTI, N. PE000023, PNRR MUR project), “Integrated Infrastructure Initiative in Photonic and Quantum Sciences” (I-PHOQS, N. IR0000016, PNRR MUR project). X.R.W. acknowledges support from Academic Research Fund Tier 2 (Grant No. MOE-T2EP50120-0006 and MOE-T2EP50220-0005) and Tier 3 (Grant No. MOE2018-T3-1-002) from Singapore Ministry of Education. K.D., T.K., and T.C. H.L., were also supported by Tier 3 (Grant No. MOE2018-T3-1-002) from the Singapore Ministry of Education. K.W. and T.T. acknowledge support from JSPS KAKENHI (Grant Numbers 19H05790, 20H00354, and 21H05233) and A3 Foresight by JSPS.

Author contributions

Z.H. conceived the ideas and designed the experiments. Z.H. prepared the microcavity samples with the help of J.Z. and Q.S. Z.H. performed the optical spectroscopy with the help of J.Z., A.F., Y.C., H.L., Y.L., and R.S. T.K. and K.D. performed the theoretical calculation. T.K. mainly performed the coupled rate equation part. J.W. and G.E. performed the PLE measurement. K.W. and T.T. prepared the hBN crystal. Z.H., T.K., A.F., K.D., X.R.W., S.G., D.S., T.C.H.L., and Q.X. wrote the manuscript with input from all authors. Q.X. supervised the project.

Competing interests

The authors declare no competing interests.

Additional information

Supplementary information The online version contains supplementary material available at <https://doi.org/10.1038/s41467-024-45554-y>.

Correspondence and requests for materials should be addressed to Zehua Hu, Kevin Dini or Qihua Xiong.

Peer review information *Nature Communications* thanks the anonymous reviewers for their contribution to the peer review of this work. A peer review file is available.

Reprints and permissions information is available at <http://www.nature.com/reprints>

Publisher's note Springer Nature remains neutral with regard to jurisdictional claims in published maps and institutional affiliations.

Open Access This article is licensed under a Creative Commons Attribution 4.0 International License, which permits use, sharing, adaptation, distribution and reproduction in any medium or format, as long as you give appropriate credit to the original author(s) and the source, provide a link to the Creative Commons licence, and indicate if changes were made. The images or other third party material in this article are included in the article's Creative Commons licence, unless indicated otherwise in a credit line to the material. If material is not included in the article's Creative Commons licence and your intended use is not permitted by statutory regulation or exceeds the permitted use, you will need to obtain permission directly from the copyright holder. To view a copy of this licence, visit <http://creativecommons.org/licenses/by/4.0/>.

© The Author(s) 2024

¹National Laboratory of Solid State Microstructures, School of Electronic Science and Engineering, and Collaborative Innovation Center of Advanced Microstructures, Nanjing University, Nanjing 210093, China. ²Centre for Quantum Technologies, National University of Singapore, Singapore 117543, Singapore. ³CNR NANOTEC Institute of Nanotechnology, Lecce 73100, Italy. ⁴Division of Physics and Applied Physics, School of Physical and Mathematical Sciences, Nanyang Technological University, Singapore 637371, Singapore. ⁵Beijing Academy of Quantum Information Sciences, Beijing 100193, P.R. China. ⁶State Key Laboratory of Low-Dimensional Quantum, Department of Physics, Tsinghua University, Beijing 100084, P.R. China. ⁷Department of Physics, National University of Singapore, Singapore 117542, Singapore. ⁸Research Center for Functional Materials, National Institute for Materials Science, 1-1 Namiki, Tsukuba 305-0044, Japan. ⁹International Center for Materials Nanoarchitectonics, National Institute for Materials Science, 1-1 Namiki, Tsukuba 305-0044, Japan. ¹⁰School of Electrical and Electronic Engineering, Nanyang Technological University, Singapore 639798, Singapore. ¹¹Frontier Science Center for Quantum Information, Beijing 100084, P.R. China. ¹²Collaborative Innovation Center of Quantum Matter, Beijing, P.R. China. ¹³These authors contributed equally: Zehua Hu, Tanjung Krisnanda, Antonio Fieramosca. ✉ e-mail: zehuah@nju.edu.cn; kdini@ntu.edu.sg; qihua_xiong@tsinghua.edu.cn